Letter Vol. 8, No. 3 / March 2021 / Optica 329

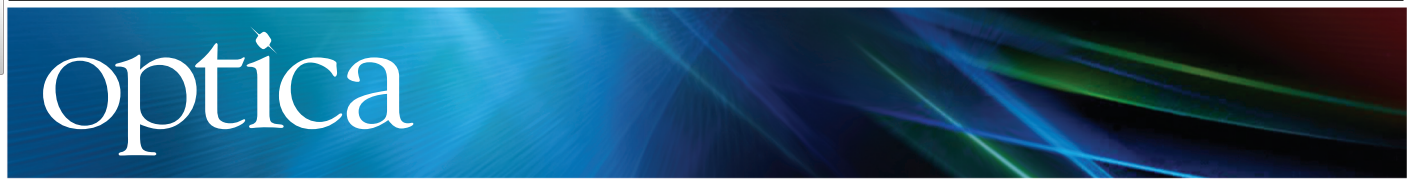

Adaptive bandwidth management for entanglement distribution in quantum networks

Navin B. Lingaraju,[1,2,*] Hsuan-Hao Lu,[1,2] Suparna Seshadri,[1,2] Daniel E. Leaird,[1,2] Andrew M. Weiner,[1,2] and Joseph M. Lukens[3]

[1]School of Electrical and Computer Engineering, Purdue University, West Lafayette, Indiana 47907, USA
[2]Purdue Quantum Science and Engineering Institute, Purdue University, West Lafayette, Indiana 47907, USA
[3]Quantum Information Science Group, Computational Sciences and Engineering Division, Oak Ridge National Laboratory, Oak Ridge, Tennessee 37831, USA
*Corresponding author: navin@purdue.edu

Received 28 October 2020; accepted 17 January 2021 (Doc. ID 413657); published 2 March 2021

Flexible grid wavelength division multiplexing is a powerful tool in lightwave communications to maximize spectral efficiency. In the emerging field of quantum networking, the need for effective resource provisioning is particularly acute, given the generally lower power levels, higher sensitivity to loss, and inapplicability of optical detection and retransmission. In this letter, we leverage flex grid technology to demonstrate reconfigurable distribution of quantum entanglement in a four-user tabletop network. By adaptively partitioning bandwidth with a single wavelength-selective switch, we successfully equalize two-party coincidence rates that initially differ by over two orders of magnitude. Our scalable approach introduces loss that is fixed with the number of users, offering a practical path for the establishment and management of quality-of-service guarantees in large quantum networks.

https://doi.org/10.1364/OPTICA.413657

Quantum technology offers the promise of dramatic computational speed up [1] and security [2] beyond the capabilities of classical resources. Within this overall landscape, the development of quantum networks is critical to interconnect quantum resources for applications such as blind quantum computing, quantum sensors, and distributed quantum computation [3]. While the specific design of such networks remains an active area of research, to the greatest extent possible any solution should integrate seamlessly into the existing fiber optic infrastructure, while also leveraging advanced techniques in modern lightwave communications.

To this end, an efficient quantum networking approach gaining traction in recent years is based on entanglement distribution by a central provider [4–10]. In this paradigm, broadband polarization-entangled photons are carved into a series of spectral slices, which are then distributed to different users in the network. Since these photons are also entangled in the time-frequency degree of freedom, nonclassical polarization correlations are shared only between users who receive energy-matched channels. Recently, Wengerowsky *et al.* [9] demonstrated a fully and simultaneously connected quantum key distribution network by multiplexing multiple spectral slices to each user such that polarization entanglement exists between every possible two-party link. This elegant demonstration relies only on passive components, namely, a hierarchical tree of dense wavelength division multiplexing (DWDM) filters. However, extending to significantly larger networks is a challenge, as the number of filters scales quadratically with the number of users N: a total of $2N^2 - 3N$ DWDMs are needed for full connectivity [9]. Follow-up work [11] made use of 50:50 beam splitters to reduce the number of DWDMs in this architecture by having two users share each spectral slice. However, this comes at the expense of higher noise due to the intrinsic loss of 3 dB splitting.

In this letter, we propose and demonstrate what we believe is a significantly improved approach to entanglement distribution. In lieu of passive optical elements, we use a wavelength-selective switch (WSS) to apportion the biphoton bandwidth between users on a network. This approach provides a clear advantage in terms of network scalability as the loss incurred during entanglement distribution is independent of the number of users. Furthermore, the bandwidth allocation can be reconfigured dynamically with simple electronic controls. Consequently, the central provider can enable not only a fully and simultaneously connected network, but any arbitrary subgraph. Finally, the bandwidth of spectral slices routed to each user can be modified, thus making it possible to boost or throttle the entanglement rate for a particular two-party link without modifying the pair source, pump laser, or physical links on the network. Until there is broader deployment of quantum networks in general, what criteria or communications priorities should guide the distribution of entanglement will remain unclear. Yet our work highlights how the use of reconfigurable bandwidth provisioning can optimize network performance with regard to a preferred criterion or outcome.

Our testbed is illustrated in Fig. 1. Time-energy entangled photons are generated by spontaneous parametric down-conversion in a 10 mm long, type II periodically poled lithium niobate ridge waveguide (PPLN, HC Photonics, Hsinchu City, Taiwan). The PPLN is pumped by a ∼24 mW continuous wave laser ($\lambda \approx 780$ nm) [12], producing biphotons with a full width at half-maximum of ∼2.5 nm (310 GHz). To generate photon pairs also entangled in polarization, we match the pump wavelength

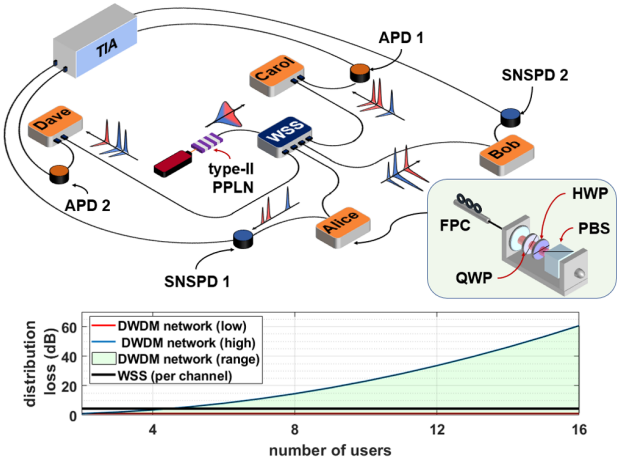

Fig. 1. Network testbed for adaptive entanglement distribution. The inset shows the spread and scaling of channel losses for an alternative DWDM approach compared to the WSS.

and PPLN temperature to ensure spectrally degenerate down conversion. Temporal walk-off between horizontally and vertically polarized components of the biphoton is compensated with a 90° splice of polarization-maintaining (PM) fiber with a proper length [13]. As a result, any two energy-matched spectral slices ($\omega_{\text{signal}} + \omega_{\text{idler}} = \omega_{\text{pump}}$) are polarization-entangled, ideally in the form $|\Psi\rangle \propto |HV\rangle + e^{i\phi}|VH\rangle$. For entanglement distribution, the output of the PPLN is sent to a WSS (WaveShaper 4000S/X, Finisar, Sunnyvale, CA, USA), which can multiplex arbitrary spectral slices across the C- and L-bands to any one of four output ports. The only limitation on this programmability is the resolution (∼20 GHz), which sets a lower bound on the bandwidth of individual slices. Subject to this bound, the WSS imparts equal losses for all connections up to the number of its output fibers.

On the other hand, the equivalent DWDM network presents widely varying loss across different channels as the number of users increases. While one channel need only travel through two DWDM filters, the worst-case spectral band must undergo, at the very least, $N^2 - N$ reflections followed by one transmission [9]. As an example, Fig. 1 (inset) compares the loss for fully connected networks assuming a typical 4.5 dB loss for the WSS and 0.25 dB (0.6 dB) for reflection (transmission) from each DWDM filter. Below four users, the DWDM approach is more efficient, but this rapidly changes as the network size increases, with a worst-case channel loss reaching 60 dB at the 16-user mark. We suspect it may be possible to design more balanced DWDM configurations that mitigate this wide loss spread, yet the fundamental quadratic scaling should still remain.

The users, identified as Alice, Bob, Carol, and Dave in Fig. 1, are each equipped with a polarization analysis module that includes a fiber-based polarization controller (FPC), a quarter-wave plate (QWP), a half-wave plate (HWP), a polarizer, and a single-photon detector. The FPC compensates for the rotation of the polarization state that occurs during the transmission between the source and the QWP. While the manual FPC can map the state of polarization from the HV basis of the source to the HV basis of the polarization analysis module, there remains an undetermined phase between the H and V states. We compensate for this unknown phase by orienting all QWPs at 45°, followed by an additional rotation of HWP settings, for polarization correlation measurements in the diagonal–antidiagonal (DA) basis [14]. The HWP angle at which maximum contrast is obtained corresponds to the effective DA basis; concretely, we set the angle such that the ideal quantum state is $|\Psi^-\rangle \propto |HV\rangle - |VH\rangle$. We note that, with additional detectors for simultaneous HV and DA monitoring [15] or automated feedback with classical reference pulses [16], it would be possible to compensate this directly with the FPC and remove the QWP.

Photons exiting the polarizer are routed to single-photon detectors for coincidence detection. Of the four detectors in our testbed, two are superconducting nanowire single-photon detectors (SNSPDs) while two are InGaAs avalanche photodiodes (APDs). The free-running SNSPDs used by Alice and Bob have quantum efficiencies of ∼0.85. The APDs, which are allocated to Carol and Dave, are gated with a 20 MHz clock (10% duty cycle) and have quantum efficiencies of ∼0.2 and ∼0.1, respectively, with afterpulsing and increased dark counts further reducing performance of the APD links compared to those terminated with SNSPDs. When the WSS is programmed to operate as a multiport (1:4) beam splitter for the whole biphoton bandwidth, the average singles count rates vary greatly among users: $2.6 \times 10^5\ \text{s}^{-1}$ (Alice), $3.3 \times 10^5\ \text{s}^{-1}$ (Bob), $5.5 \times 10^3\ \text{s}^{-1}$ (Carol), and $3.3 \times 10^3\ \text{s}^{-1}$ (Dave).

Prior to apportioning the biphoton bandwidth for entanglement distribution over the network, we characterize the entanglement after the WSS using Alice's and Bob's polarization analysis modules. The biphoton spectrum is carved into 24 spectral slices, each of which is 24 GHz wide, and includes a central stopband, as shown in Fig. 2(a). This channel width is chosen to match an integer multiple of the effective 4 GHz addressability of the WSS (owing to how pixels in the device's spatial light modulator are wired together) while still exceeding its ∼20 GHz spectral resolution. We define a channel as a pair of such energy-matched spectral slices. Fidelity with respect to the $|\Psi^-\rangle$ Bell state is determined by measurements in two sets of mutually unbiased bases [coincidences in HV and DA bases are shown in Fig. 2(b)]. Despite the tomographic incompleteness of this two-basis pair

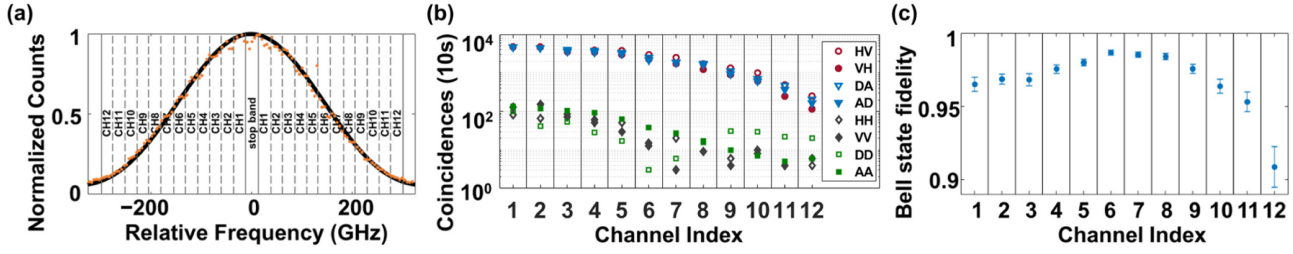

Fig. 2. (a) Sinc-squared fit to the normalized singles rate as a function of detuning from the center of the biphoton spectrum. (b) Polarization-correlation measurements in the rectilinear (HV) and diagonal (DA) bases, measured between Alice and Bob for all 12 channels. (c) Bell state fidelities computed using Bayesian quantum state tomography (without accidental subtraction).

set, our use of Bayesian mean estimation [17] nevertheless enables us to obtain meaningful state estimates, which due to the high correlations obtained also contain low uncertainty. Our measurement results using the Bayesian tomography workflow of [18] are presented in Fig. 2(c). For channels 1–11, which span most of the biphoton bandwidth, we are able to measure fidelities higher than 95%, which illustrates both the quality of polarization rotation compensation and the stability of the WSS's polarization diversity scheme. While a valuable initial assessment, we note that this characterization does not guarantee the fidelities of arbitrary groupings of these channels. Due to a combination of effects such as crosstalk, multipair emission, and frequency-dependent birefringence, any allocation should be tested in situ for performance on a given network, an important practical consideration for field implementation.

The four-user network illustrated in Fig. 1 comprises six possible two-party connections, called links, each of which is assigned a unique color in Fig. 3. The down-converted photons pass to the WSS for wavelength-multiplexed distribution to Alice, Bob, Charlie, and Dave, and we add suitable electronic offsets to the outputs of each detector to position the coincidence peaks for all six links in multiples of 10 ns apart. We use a coincidence window of 1024 ps, which exceeds the jitter of all detector pairs.

We first consider the case of wavelength-multiplexed entanglement distribution based on a fixed 48 GHz grid, corresponding to a total of six equal-width pairs from the 12 channels defined in Fig. 2(a). The biphoton bandwidth, counting from the center out, is allocated to the different links based on alphabetical ordering [i.e., Alice–Bob (AB), Alice–Carol (AC), Alice–Dave (AD), Bob–Carol (BC), Bob–Dave (BD), and Carol–Dave (CD)]. Figure 3(a) shows two-photon events recorded between all six links. Note the extremely low counts of link CD, due to the fact it combines the two least efficient channels and, under this distribution scenario, also receives the pair of 48 GHz spectral slices with the lowest flux. While far from optimal in terms of balancing two-party coincidence rates, this configuration might alternatively be interpreted as boosting service for a premium link (AB in this case). Thus, we see the value of flexible bandwidth allocation in configuring the network for different needs, such as diverse quality-of-service targets. Nevertheless, to better balance coincidence rates across all six links, we next reallocate the biphoton bandwidth on the same fixed 48 GHz spectral grid. Now, brighter slices are routed to the less efficient links. Figure 3(b) shows histograms of two-photon events for all user-to-user connections. While the previous scenario saw a ratio of ∼4200 in the coincidence rates of links AB and CD, that imbalance is now only ∼26.

Moving from fixed-grid distribution to a more flexible provisioning of bandwidth, we finally use the 12 channels defined in Fig. 2(a), without any limitations on how they are allocated between the different links. To equalize the coincidence rates across the network, we provision the spectrum as shown in Fig. 3(c); we no longer enable a fully connected network because link CD would not even in the most favorable allocation (sending seven channels with the highest pair flux) be able to reach coincidence rates comparable to the other users. Therefore, we program the WSS to harmonize the coincidence rate among a subgraph of five links (all links except for CD). From Fig. 3(c) we see that all coincidence rates are within a factor of 2, a significant improvement over the fixed-grid cases.

Importantly, for the allocations of Figs. 3(b) and 3(c), balancing coincidence rates relies not only on link bandwidth, but also use of the full biphoton spectrum [Fig. 2(a)], which is a departure from previous works that limited consideration to uniform-flux slices near the center of the spectrum [9,11]. In our full-flex scenario in particular, interleaving channel allocations (e.g., for links AC/BC and AD/BD) thereby allows us to equalize the mean flux for links of comparable detection efficiencies. While high flux across a broader bandwidth would always be preferred, our results show the value of flex-grid allocation under the constraints of limited entanglement resources in a network.

Moving forward, our approach should be readily extendable to many more users with only small modifications to the basic setup. While type-II phase matching allows us to generate polarization-entangled photon pairs in a single-pass, single-crystal configuration, alternative sources based on type-0 or type-I nonlinear crystals (co-polarized signal and idler) using Sagnac [4,19] or Mach–Zehnder [6,20] arrangements would enable the generation of polarization-entangled photon pairs with essentially uniform flux across the entire C-band. Coupled with current commercial WSSs with 20 output ports, 4.8 THz bandwidth, and 6.25 GHz

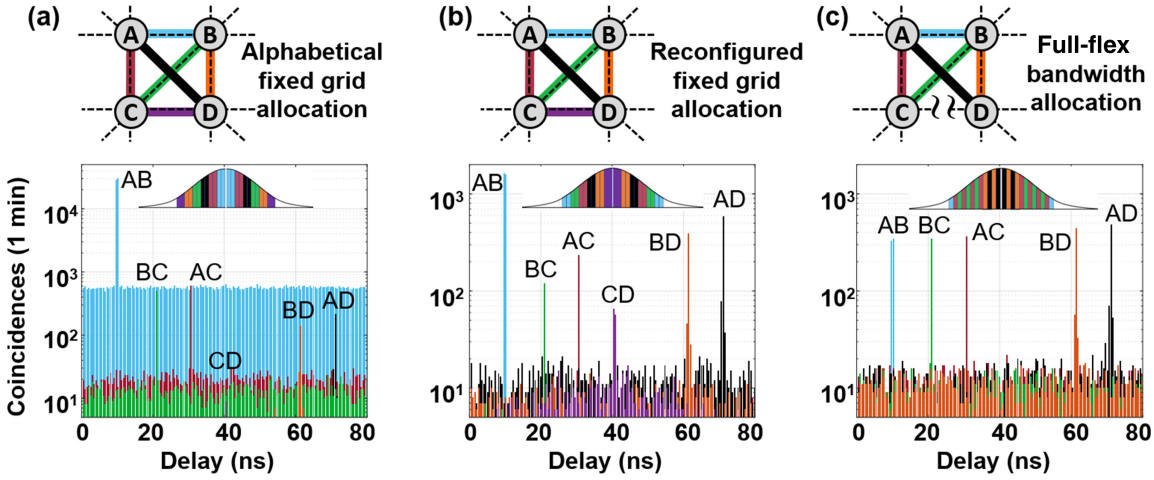

Fig. 3. (a) Coincidences for each two-party link based on a fixed 48 GHz grid, allocated alphabetically. The inset illustrates how the biphoton bandwidth is shared between all six links. (b) Coincidences for a fixed 48 GHz grid with channels allocated to best balance rates among all links. (c) Full-flex configuration with 24 GHz wide spectral slices allocated freely between users to harmonize coincidence rates across a subgraph of the network. Link CD (APD–APD) is unable to be equalized and is dropped.

resolution [21], a partitioning of 12.5 GHz slices would provide all $N(N-1)$ spectral channels necessary for a fully connected network of $N=20$ users. This stands in stark contrast to the nested DWDM approach [9], for which increasing to 20 users would require a massive 740 DWDMs. Moreover, while a 20-user WSS could support full simultaneous connectivity, its ability to reconfigure bandwidth means it is not required; the service provider can adjust bandwidth channels on demand to realize any network subgraph, allocating unused bandwidth to increase entanglement rates in other channels. Such adaptivity makes the WSS approach superior in terms of latent resources compared to passive configurations.

In the present experiment, our quality-of-service metric focused on the coincidence rate between each pair of users. Although indicative of network performance, it does not directly reflect state fidelity, which is crucial to quantum information protocols. Similarly, the application of our technique to a deployed quantum network will demand precise clock synchronization between spatially separated nodes, a challenge absent in the present tabletop experiment. In future work, we are looking to improve on both limitations, using state tomography to quantify the entanglement of each link in terms of ebits/s and synchronizing nonlocal time taggers via an additional classical network layer. Finally, while we use frequency entanglement here to establish bipartite correlations—with polarization as the information carrier—it is also possible to leverage the frequency degree of freedom directly for quantum information processing [22,23]. While typically considered in a single-polarization context, recent demonstrations of polarization-diversity phase modulation [24,25] indicate the potential to exploit both frequency and polarization in parallel for carrying and processing quantum information for even more flexible quantum networks.

Funding. Oak Ridge National Laboratory (Laboratory Directed Research and Development); U.S. Department of Energy, Office of Science, Advanced Scientific Computing Research (Early Career Research Program); National Science Foundation (1747426-DMR, 1839191-ECCS).

Acknowledgment. Preliminary results were presented at CLEO 2020 (FTh5D.2). The authors thank P. Imany, M. Alshowkan, B. Qi, and N. A. Peters for discussions, and N. Knight and O. E. Sandoval for laboratory assistance. A portion of this work was performed at Oak Ridge National Laboratory, operated by UT-Battelle for the U.S. Department of Energyy under contract no. DE-AC05-00OR22725.

Disclosures. The authors declare no conflicts of interest.

REFERENCES

1. T. D. Ladd, F. Jelezko, R. Laflamme, Y. Nakamura, C. Monroe, and J. L. O'Brien, Nature **464**, 45 (2010).
2. N. Gisin and R. Thew, Nat. Photonics **1**, 165 (2007).
3. S. Wehner, D. Elkouss, and R. Hanson, Science **362**, eaam9288 (2018).
4. H. C. Lim, A. Yoshizawa, H. Tsuchida, and K. Kikuchi, Opt. Express **16**, 22099 (2008).
5. M. Brodsky and M. D. Feuer, "Architecture for reconfigurable quantum key distribution networks based on entangled photons directed by a wavelength selective switch," U.S. patent US8311221B2 (13 November 2009).
6. I. Herbauts, B. Blauensteiner, A. Poppe, T. Jennewein, and H. Hübel, Opt. Express **21**, 29013 (2013).
7. A. Ciurana, V. Martin, J. Martinez-Mateo, B. Schrenk, M. Peev, and A. Poppe, IEEE J. Sel. Top. Quantum Electron. **21**, 6400212 (2015).
8. D. Aktas, B. Fedrici, F. Kaiser, T. Lunghi, L. Labonté, and S. Tanzilli, Laser Photon. Rev. **10**, 451 (2016).
9. S. Wengerowsky, S. K. Joshi, F. Steinlechner, H. Hübel, and R. Ursin, Nature **564**, 225 (2018).
10. E. Y. Zhu, C. Corbari, A. Gladyshev, P. G. Kazansky, H.-K. Lo, and L. Qian, J. Opt. Soc. Am. B **36**, B1 (2019).
11. S. K. Joshi, D. Aktas, S. Wengerowsky, M. Lončarić, S. P. Neumann, B. Liu, T. Scheidl, G. C. Lorenzo, Ž. Samec, L. Kling, A. Qiu, M. Razavi, M. Stipčević, J. G. Rarity, and R. Ursin, Sci. Adv. **6**, eaba0959 (2020).
12. G. Fujii, N. Namekata, M. Motoya, S. Kurimura, and S. Inoue, Opt. Express **15**, 12769 (2007).
13. F. Kaiser, A. Issautier, L. A. Ngah, O. Dănilă, H. Herrmann, W. Sohler, A. Martin, and S. Tanzilli, New J. Phys. **14**, 085015 (2012).
14. N. Peters, J. Altepeter, E. Jeffrey, D. Branning, and P. Kwiat, Quantum Inf. Comput. **3**, 503 (2003).
15. A. Poppe, A. Fedrizzi, R. Ursin, H. R. Böhm, T. Lorünser, O. Maurhardt, M. Peev, M. Suda, C. Kurtsiefer, H. Weinfurter, T. Jennewein, and A. Zeilinger, Opt. Express **12**, 3865 (2004).
16. A. Treiber, A. Poppe, M. Hentschel, D. Ferrini, T. Lorünser, E. Querasser, T. Matyus, H. Hübel, and A. Zeilinger, New J. Phys. **11**, 045013 (2009).
17. R. Blume-Kohout, New J. Phys. **12**, 043034 (2010).
18. J. M. Lukens, K. J. H. Law, A. Jasra, and P. Lougovski, New J. Phys. **22**, 063038 (2020).
19. P. Vergyris, F. Kaiser, E. Gouzien, G. Sauder, T. Lunghi, and S. Tanzilli, Quantum Sci. Technol. **2**, 024007 (2017).
20. A. Yoshizawa and H. Tsuchida, Appl. Phys. Lett. **85**, 2457 (2004).
21. Finisar, "Single wavelength selective switch (WSS)," 2020, https://finisarwss.com/wp-content/uploads/2020/07/FinisarWSS_Single_Wavelength_Selective_Switch_ProductBrief_Jun2020.pdf.
22. J. M. Lukens and P. Lougovski, Optica **4**, 8 (2017).
23. H.-H. Lu, A. M. Weiner, P. Lougovski, and J. M. Lukens, IEEE Photon. Technol. Lett. **31**, 1858 (2019).
24. O. E. Sandoval, N. B. Lingaraju, P. Imany, D. E. Leaird, M. Brodsky, and A. M. Weiner, Opt. Lett. **44**, 1674 (2019).
25. N. B. Lingaraju, N. O'Malley, D. E. Jones, O. E. Sandoval, H. N. Azzouz, D. E. Leaird, J. M. Lukens, M. Brodsky, and A. M. Weiner, in *Conference on Lasers and Electro-Optics/Quantum Electronics and Laser Science Conference (CLEO: QELS)* (Optical Society of America, 2020), paper FF1D.5.